

RESEARCH ARTICLE

10.1002/2017JC012945

Velocity and Drag Evolution From the Leading Edge of a Model Mangrove Forest

Maria Maza^{1,2} , Katherine Adler², Diogo Ramos², Adrian Mikhail Garcia² , and Heidi Nepf² ¹Environmental Hydraulics Institute (IH Cantabria), Universidad de Cantabria, Santander, Spain, ²Department of Civil and Environmental Engineering, Massachusetts Institute of Technology, Cambridge, MA, USA

Key Points:

- A mangrove forest model based on the *Rhizophora* morphology was built at 1/12th scale. Each model tree included 24 prop roots
- Velocity and TKE evolution from the forest leading edge to the fully developed region was determined by the distribution of frontal area
- Forces measured on individual mangroves decreased from the leading edge, but reached an almost constant value in the fully developed region

Supporting Information:

- Supporting Information S1

Correspondence to:

M. Maza,
mazame@unican.es

Citation:

Maza, M., Adler, K., Ramos, D., Garcia, A. M., & Nepf, H. (2017). Velocity and drag evolution from the leading edge of a model mangrove forest. *Journal of Geophysical Research: Oceans*, 122. <https://doi.org/10.1002/2017JC012945>

Received 31 MAR 2017

Accepted 24 OCT 2017

Accepted article online 2 NOV 2017

Abstract An experimental study of unidirectional flow through a model mangrove forest measured both velocity and forces on individual trees. The individual trees were 1/12th scale models of mature *Rhizophora*, including 24 prop roots distributed in a three-dimensional layout. Thirty-two model trees were distributed in a staggered array producing a 2.5 m long forest. The velocity evolved from a boundary layer profile at the forest leading edge to a vertical profile determined by the vertical distribution of frontal area, with significantly higher velocity above the prop roots. Fully developed conditions were reached at the fifth tree row from the leading edge. Within the root zone the velocity was reduced by up to 50% and the TKE was increased by as much as fivefold, relative to the upstream conditions. TKE in the root zone was mainly produced by root and trunk wakes, and it agreed in magnitude with the estimation obtained using the Tanino and Nepf (2008) formulation. Maximum TKE occurred at the top of the roots, where a strong shear region was associated with the change in frontal area. The drag measured on individual trees decreased from the leading edge and reached a constant value at the fifth row and beyond, i.e., in the fully developed region. The drag exhibited a quadratic dependence on velocity, which justified the definition of a quadratic drag coefficient. Once the correct drag length-scale was defined, the measured drag coefficients collapsed to a single function of Reynolds number.

1. Introduction

In coastal regions around the world, continuous socioeconomic development, sea level rise, and increasing storm intensity are leading to an increased risk of environmental and socioeconomic damages. Coastal managers have become interested in solutions with low environmental impact, or nature-based solutions, as an alternative to conventional hard coastal protection structures (e.g., Sutton-Grier et al., 2015). The 2014 report of the Intergovernmental Panel on Climate Change (IPCC Working Group II, 2014) highlights the important role of ecosystem-based coastal protection, including the use of mangroves and salt marshes as a buffer against damage to coastal communities. Several studies have reported the coastal protection provided by mangrove forests (Narayan et al., 2016; Vo-Luong & Massel, 2008; Yanagisawa et al., 2009). Furthermore, mangrove ecosystems provide other services such as nursery areas and fish production, biodiversity, recreation, and carbon sequestration (Barbier et al., 2011; Mitsch & Gosselink, 2015). These additional ecosystem benefits increase the services provided by mangrove forests, making them a more appealing option for coastal managers (de Groot et al., 2012). In addition, recent studies have proved that for the same level of protection, defense projects using mangroves can be several times cheaper than conventional submerged breakwaters (Narayan et al., 2016).

Mangrove forests exist in intertidal areas of tropical zones and most are characterized by a complex root system, which attenuates flow energy (Mazda et al., 1997). Among the mangrove species, *Rhizophora* represents approximately 90% of the world mangrove distribution (Ohira et al., 2013), and this species is used in the majority of restoration projects. *Rhizophora* plants are characterized by their prop roots, which form a network above the substrate. However, there is a lack of knowledge regarding the hydrodynamics within these complex root systems, and the forces exerted by the flow on the tree elements. Without this understanding, it is difficult to accurately predict the impact of proposed restoration efforts.

Several experimental studies have been performed in the last decade to characterize the interaction of different flow regimes with rigid cylinders representing mangrove trees (Ba Thuy et al., 2009; Huang et al.,

2011; Irtem et al., 2009). However, only a few studies have considered the complex structure of real mangrove trees. Ismail et al. (2012) modeled the mangrove roots using a porous plastic, considering a root porosity equal to 0.93 as representative of *Rhizophora*, and showed that the mangrove roots contributed more than the trunks and branches in reducing runup from a solitary wave. Strusinska-Correia et al. (2013) studied tsunami damping by mangroves using tree models with cylinders distributed in different layers to account for the prop roots, considering values of root density of a 5 year old *Rhizophora* mangrove. They measured solitary wave free surface evolution along the forest and forces exerted on different individual trees, showing a high decay of the force after the first three rows. Neither of these studies measured velocity profiles along the forest. Recently, Zhang et al. (2015) constructed 1:7.5 scale trees based on field surveys of *Rhizophora*, with prop roots constructed from aluminum rods. They measured velocity and used a force balance to infer the flow resistance. However, they did not directly measure force on the tree models, and their tree models were distributed along the flume without any overlap between the root zones of adjacent trees, which is not representative of real tree growth.

A better understanding of the flow adjustment and hydrodynamic drag within the complex mangrove geometry will enable a better quantification of coastal protection provided by these ecosystems. This information is required to accurately evaluate the services provided by mangrove forests, which can facilitate coastal management decisions. Here an experimental study of unidirectional flow through a model mangrove forest was performed to characterize the flow adjustment from the leading edge and the drag forces exerted on individual trees. Unidirectional currents were chosen as representative of storm surge events. During storm surge velocity varies over time scales of minutes to hours, which is long enough to represent quasi steady flow within the forest. Waves, although sometimes significant in considerations of coastal protection, were not considered. Each model tree included a geometrically accurate prop root system. A description of the mangrove model and mangrove forest is presented in section 2. Section 3 describes the experimental setup and methods. The results are discussed in section 4, and the important conclusions are drawn in section 5.

2. Geometry and Scaling of Model Mangrove Forest

Mangroves have a complex structure formed by aerial roots, trunks, and branches, and it is important to study accurate geometries to provide the best assessment of coastal protection. Ohira et al. (2013) provides a detailed three-dimensional geometric model of stilt root morphology based on a collection of field measurements. The geometry of the root system depends on the diameter of the main trunk at breast height (DBH), which is also an indication of tree age. In this study, we consider mature mangroves for which $DBH = 0.20$ m (Alongi, 2008). According to the Ohira scaling, for $DBH = 0.20$ m the highest root attaches to the trunk at $HR_{max} = 2.012$ m, and the number of roots is $N = 24$. These geometric values are in the same range as the maximum root height and number of roots per tree reported by Méndez-Alonzo et al. (2015). The diameter of these roots range from 0.033 to 0.042 m. The roots are distributed around the trunk at eight different angles leading to the three-dimensional layout shown in Figure 1.

The model mangrove forest was built at 1:12 scale. This scale was chosen to fit the mangrove forest into the test section at the desired mangrove geometry and trunk density. The mangrove roots were built using a computer numerical control (CNC) wire-bending machine (DIWire, Pensa Labs). Roots were represented by brass rods of 3.175 mm diameter, corresponding to the mean root diameter of the 24 roots at real scale (3.8 cm). The mangrove trunks were constructed from acrylic tubes of 1.6 cm diameter, corresponding to 20 cm at real scale. The acrylic tubes were drilled using a programmable drill machine at the heights described by Ohira et al. (2013) for the 24 roots and forming the three-dimensional layout presented in Figure 1. The maximum root height in the model was $HR_{max} = 16.8$ cm. Both the root and trunk materials were rigid enough to represent real mangrove stiffness, according to values reported by Zhang et al. (2015). Two versions of the model mangrove were built: full trees with 24 roots and half trees with 15 roots. The half trees were located next to the flume walls to uniformly cover the test section width and to avoid accelerated flows along the walls. A total of 20 whole trees and 12 half trees were built, using 32 trunks and 660 roots. The mangroves were attached to the bottom of the flume using perforated acrylic baseboards into which the mangrove trunks were inserted. Figure 2 shows one whole mangrove and the mangrove forest inside the flume. The distance between each row of trunks, w , was equal to 0.208 m (shown in Figure 5).

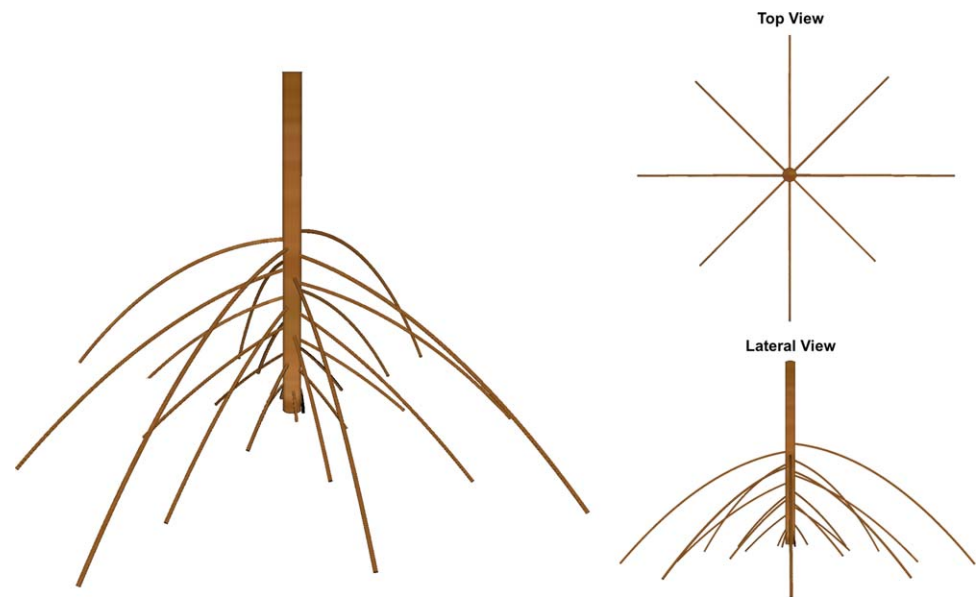


Figure 1. Three-dimensional stilt root morphology of a *Rhizophora* mangrove based on Ohira et al. (2013).

The trees were distributed in a staggered configuration leading to a mangrove density equal to 10.4 trees/m² (722 trees/ha at real scale). This density was chosen based the density reported in Ward et al. (2006) for a typical *Rhizophora* forest, specifically around 600 trees/ha.

The frontal area of an individual mangrove tree was measured using image analysis. A mangrove model was photographed against a white background. Five photos were taken, considering five different angles of rotation. The frontal area was evaluated using the Matlab image processing toolbox to convert the image into a binary file and counting the black pixels representing the mangrove. A conversion factor from pixels to unit length was determined using as reference the trunk diameter in the horizontal direction and the height of the highest root in the vertical direction. As an example, one mangrove image is shown in the left plot of Figure 3, and the frontal area within each 1 cm vertical slice is shown in the right plot of Figure 3. The horizontal bars indicate the variability associated with tree orientation. The frontal area per tree (A) can be estimated by integrating this curve over the water depth. The frontal area per unit volume $a = An/h$, with n the number of trees per bed area (here, $n = 10.4$ trees m⁻²) and h the water depth. The frontal area per volume varied with flow depth from $a = 0.58$ to 1.03 m⁻¹.

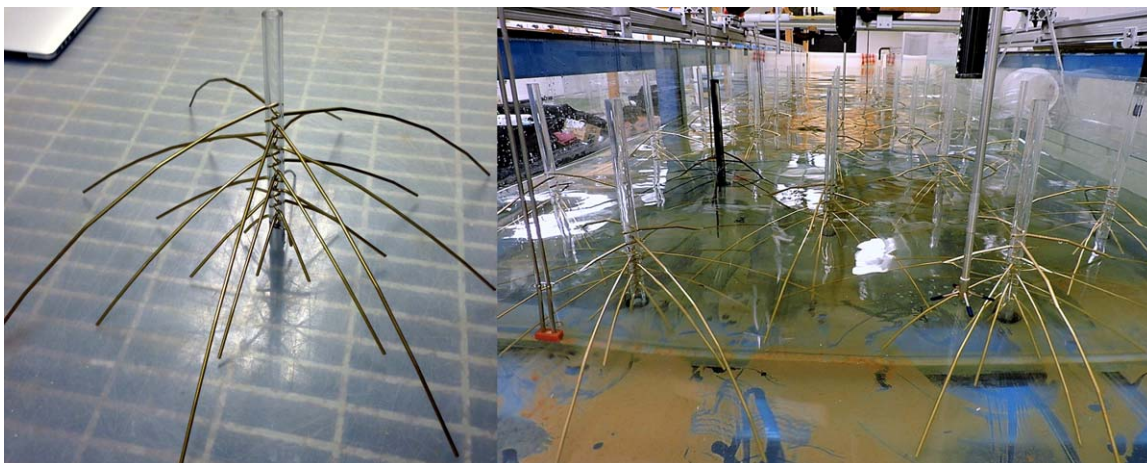


Figure 2. (left plot) 1/12th scale model mangrove built using brass rods and an acrylic tube and (right plot) mangrove forest inside the flume.

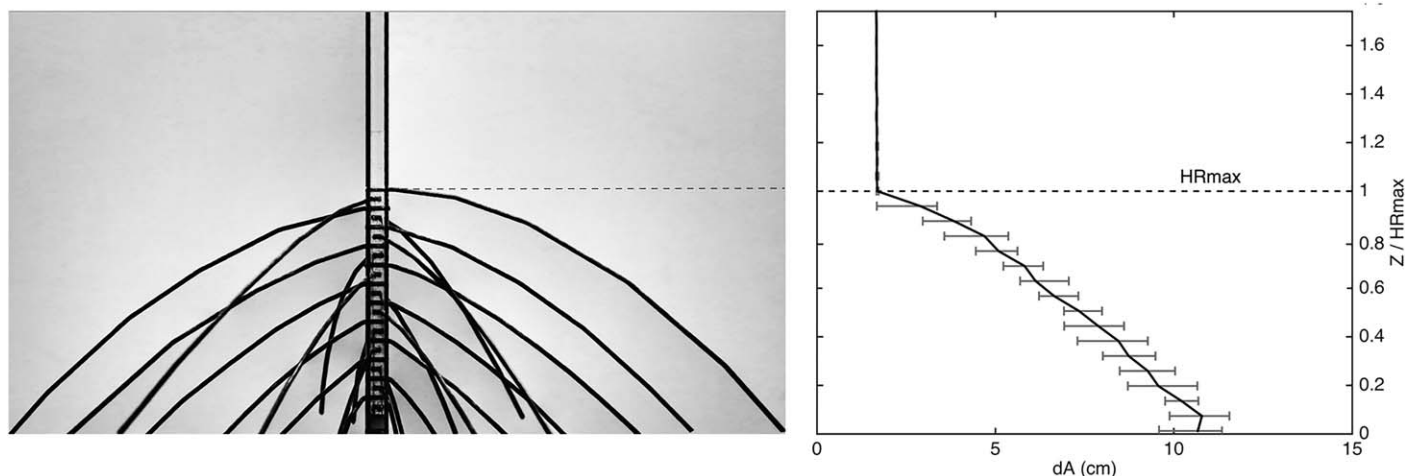


Figure 3. The left plot shows the original image of one mangrove model. The right plot shows the vertical profile of tree frontal area per cm vertical interval, dA (cm). The vertical position (z) is normalized by the maximum root height, $HR_{max} = 16.8$ cm. The horizontal bars indicate the variability associated with different tree orientation.

Froude number, F_n , similarity was used to select the model system velocity, U_M , based on the real velocity, U_R :

$$F_n = \frac{U_M}{\sqrt{gL_M}} = \frac{U_R}{\sqrt{gL_R}} \quad (1)$$

in which g is the acceleration of gravity. As noted above, the ratio of model length-scales (L_M) to real length-scale (L_R) was $L_M/L_R = 1/12$. Using this ratio in (1), $U_M = 0.29U_R$. In addition, the Reynolds number, Re , in the model should be high enough to ensure similarity in wake structure between the model and the real conditions. The Reynolds numbers based on both trunk and root diameters were considered:

$$Re_{trunk} = \frac{U_M D_{trunk}}{\nu} \quad \& \quad Re_{roots} = \frac{U_M D_{roots}}{\nu} \quad (2)$$

in which D_{trunk} and D_{roots} are the trunk and root diameter, respectively, and ν is the kinematic viscosity. Storm surge conditions can produce velocities around 0.5 m/s (e.g., Roeber et al., 2015), which corresponds to 0.144 m/s at model scale. This velocity produced $Re_{trunk} = 2,405$ and $Re_{roots} = 457$, which were high enough to ensure turbulent wakes ($Re > 200$), which would be consistent with field conditions. However, the model study covered a range of velocities ($U_M = 3\text{--}20$ cm/s), and for $U_M < 6$ cm/s the root Reynolds number was below 200. For those specific cases, root wakes were laminar and we cannot ensure similarity.

3. Flume Experiments

The experiments were conducted at the MIT Laboratory in a 1.2 m wide and 12.2 m long recirculating glass flume with horizontal bed. To generate higher currents, the test section width was narrowed to $B = 1$ m by inserting acrylic walls, as displayed in the middle plot in Figure 4. The mangrove forest began 5 m from the flume inlet and was 2.5 m long.

Flow discharge, Q , was controlled by a variable-speed pump and measured using a flow meter. The water depth, h , was measured in front of the forest using a free surface gauge. By changing the gate height at the end of the flume the water depth (h) was adjusted between 9 and 25 cm, which included water depths both above and below the maximum root height, $HR_{max} = 16.8$ cm. Vertical profiles of velocity were measured using three Acoustic Doppler Velocimeters (ADV), which were mounted to vertical rods that moved vertically with an increment of 1 cm. ADV1 was used to measure the velocity profile at the forest leading edge (see Figure 5). The other two ADVs were located within the fully developed flow region. The fully developed flow region was identified by taking velocity measurements at increasing distance from the forest leading edge. The vertical profiles of velocity progressively evolved from the leading edge

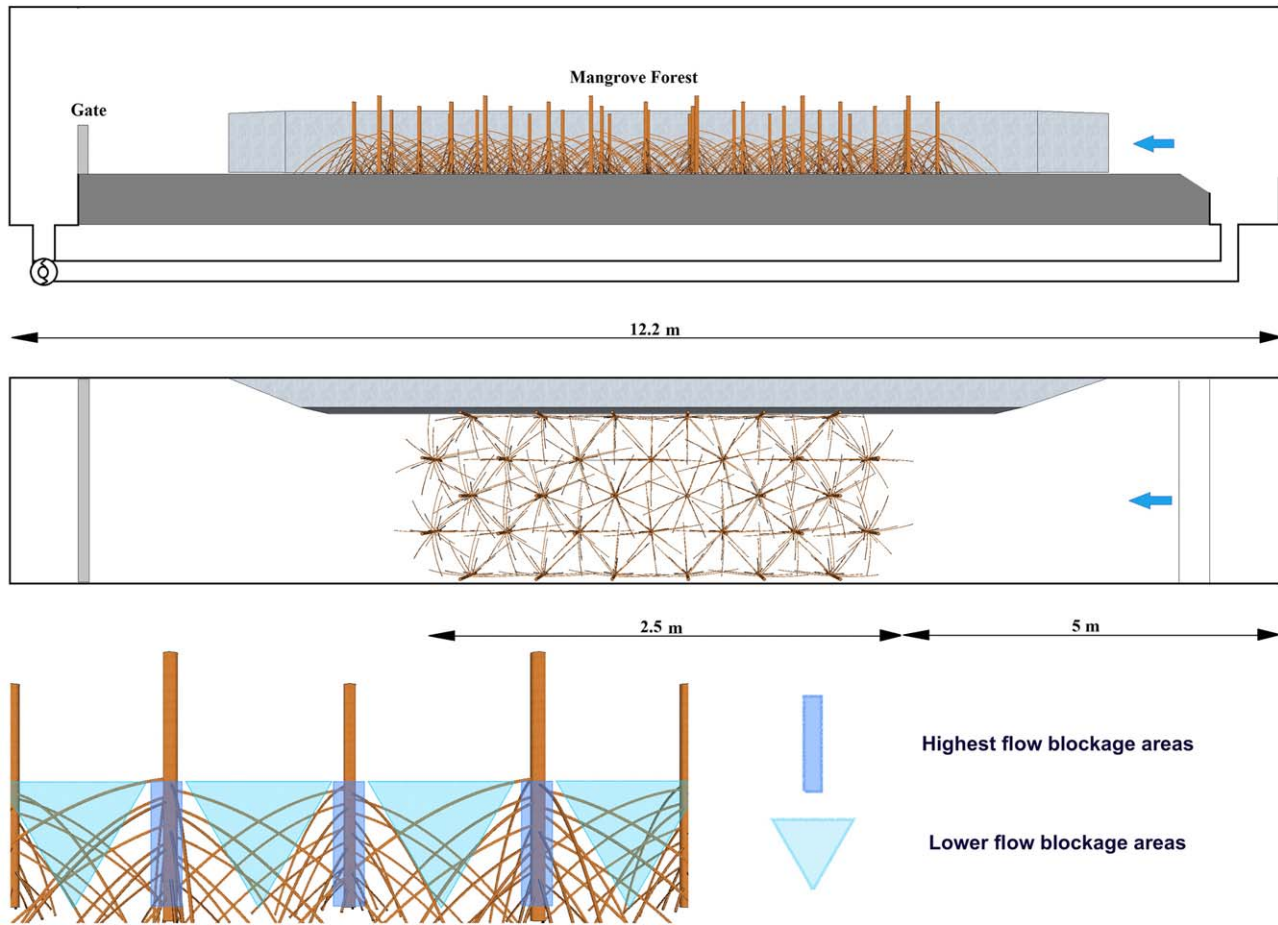


Figure 4. Schematic diagram of side and top view of the flume, in top and middle plot, respectively. Middle plot shows the distribution of 20 whole and 12 half trees in the flume. Two first rows frontal view is shown in detailed in the bottom plot differentiating between areas of higher and lower flow blockage. Figure is not to scale.

until row 5, and beyond this point the profiles reached their fully developed shape. This progression is illustrated in the left plot of Figure 11, which is discussed in the next section. Based on the evolution of velocity, ADV2 and ADV3 were located inside the fully developed flow region. ADV3 was mounted on a

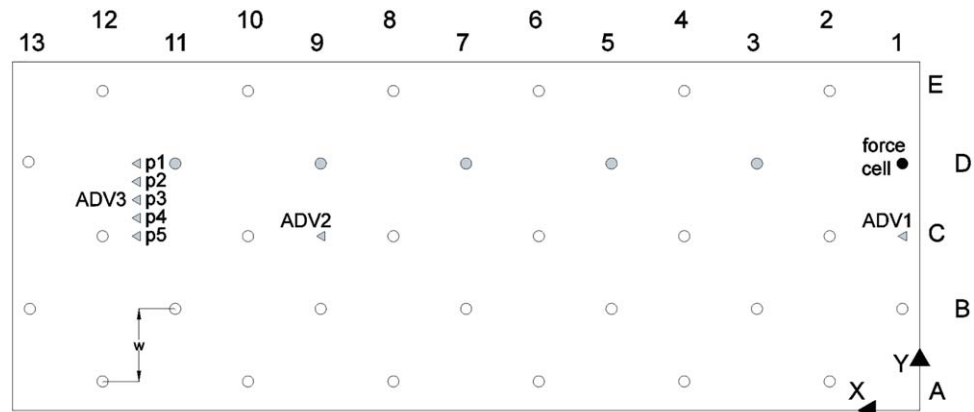


Figure 5. Individual mangrove trunks (represented by small circles) were arranged in rows 1–13 in the x direction, measured from the leading edge of the forest, and rows A to E in the y direction. Gray triangles represent ADV locations. The black dot indicates the mangrove at the leading edge attached to the force cell. Gray dots indicate the additional positions where force and velocity measurements were made in the second set of experiments.

lateral worm screw and traversed to collect velocity profiles at five lateral locations, each 5 cm apart (positions p1 to p5 in Figure 5).

Three components of instantaneous velocity (u , v , w) corresponding to (streamwise, lateral, vertical) components, respectively, were collected at each ADV measurement position. At each point the velocity was sampled at 25 Hz for 3 min. Using a matlab script, the velocity records were despiked following Goring and Nikora (2002). Each velocity record was decomposed into time-averaged components (\bar{u} , \bar{v} , \bar{w}) and fluctuating components (u' , v' , w'). The turbulent kinetic energy, TKE, was obtained as:

$$\text{TKE} = \frac{1}{2} (\overline{u'^2} + \overline{v'^2} + \overline{w'^2}) \quad (3)$$

Forces were measured in two separate experiments. First, forces on the first mangrove in row D were measured at flow speeds between 3 and 20 cm/s and flow depths between 9 and 25 cm. In a second set of experiments, the force exerted on mangroves 1–11 located in row D were measured at different flow rates for $h > HR_{max}$. After measuring the force at each position, the mangrove was removed and the velocity was measured at the same location. Because the original baseboard began to warp, a replacement baseboard was introduced before the second set of force measurements. With the new baseboard, the trunk spacing increased slightly (by 4%) from $w = 0.208$ cm to 0.216 m. Based on comparisons between replicate measurements before and after the new baseboard was introduced, this change had negligible impact on measurements.

Forces were measured using a 100 g Futek force transducer. The device was calibrated weekly using weights of known mass, which consistently produced a linear calibration curve between strain and force. To eliminate the tree weight from the force measurement, the test mangrove was mounted onto a pivot arm, which supported the mangrove weight, with the other end of the pivot arm connected to the force transducer (Figure 6). The distance from the pivot point to the force transducer, L_{LC} , was 17.0 cm, and the distance from the pivot point to the flume bed, L_B , was 32.5 cm. Note that the roots of the tree mounted on the pivot were shaved slightly so that the tree made no contact with the bed. The gap between the roots and the bed was less than 0.5 cm.

Forces recorded by the load cell (F_{LC}) were converted to drag force on the tree (F_D) using a balance of torque:

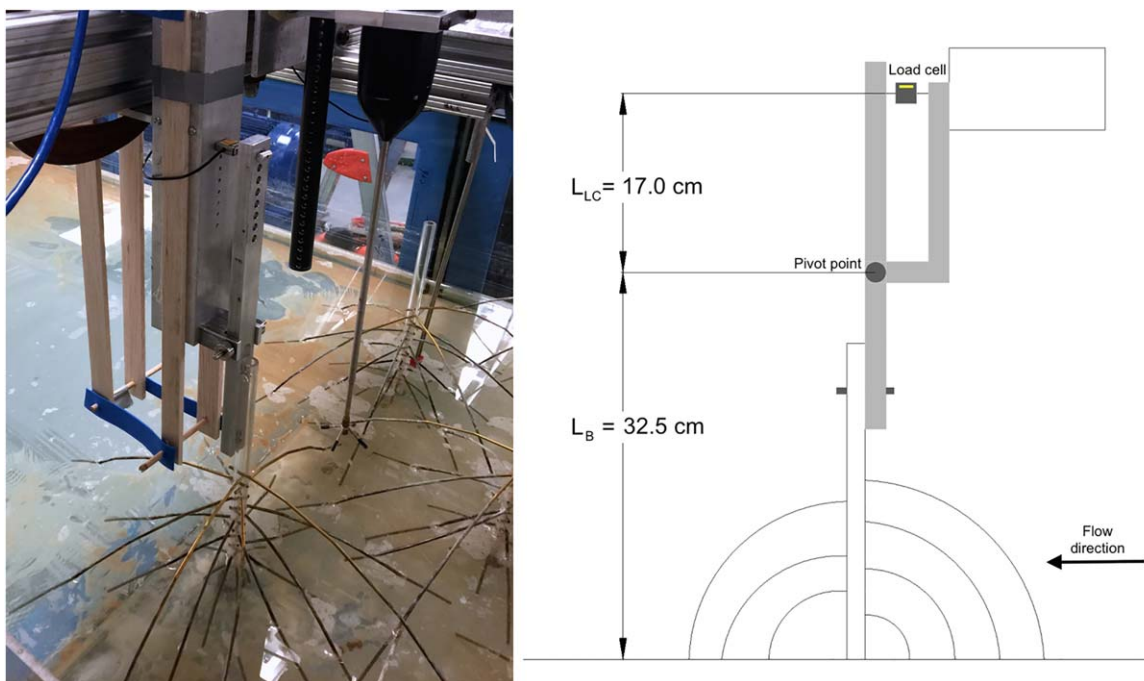


Figure 6. Force transducer setup using a pivot arm to eliminate the tree weight from the force measurement. The left plot shows the test mangrove mounted in the flume. The right plot provides a sketch of the relative position of the different elements.

$$F_D = \frac{F_{LC} L_{LC}}{L_D} \quad (4)$$

in which L_D was the distance from the pivot point to the centroid of the force exerted on the mangrove. The centroid of force was estimated using the vertical profiles of measured time-average velocity (\bar{u}) and frontal area (dA , Figure 3).

$$L_D = L_B - \frac{\int_0^h F_D(z) z dz}{\int_0^h F_D(z) dz} = L_B - \frac{\sum_{i=0}^h dA(i) \bar{u}^2(i) z(i)}{\sum_{i=0}^h dA(i) \bar{u}^2(i)} \quad (5)$$

Following previous studies in the literature (e.g., Dalrymple et al., 1984; Kobayashi et al., 1993; Losada et al., 2016; Méndez et al., 1999), we assumed that the drag coefficient, C_D , was constant along the vertical. This is an appropriate choice, given that only the total force was measured, and not a distribution of forces along the vertical. Further, previous studies of cylinder drag have shown that between $Re = 10^2$ and 10^5 the drag coefficient is nearly constant ($\pm 20\%$, e.g., Munson et al., 2013). Even though velocity varied in the vertical, the Re value fell mostly in this range, making it reasonable to assume a constant C_D . By assuming a vertically constant C_D , this coefficient was cancelled from (5), so that L_D could be estimated without a priori knowledge of C_D .

4. Experimental Results and Discussion

4.1. Velocity and Turbulent Kinetic Energy

Time-averaged, streamwise velocity, \bar{u} , and TKE profiles measured for two of the water depths ($h = 25.0$ and 14.9 cm), with channel-average velocity $U = Q/Bh$ of 9.0 and 16.7 cm/s, respectively, are shown in Figures 7 and 8. The velocity was normalized by U , and TKE was normalized by U^2 . The figures compare profiles at the leading edge of the forest (blue symbols) to multiple streamwise (Figure 7) and lateral (Figure 8) positions within the fully developed region of the forest (gray symbols). First, the velocity profiles within the forest were significantly altered from the profile at the leading edge. Upstream of the forest, the velocity profile (blue symbols) was determined by the bed drag and followed a boundary layer shape. Within the forest, the shape of the velocity profile was predominantly determined by the drag associated with the trees, and thus was higher in regions of lower frontal area. For example, for water depth $h = 25$ cm (Figure 7a), which was higher than the root zone ($HR_{max} = 16.8$ cm), the velocity was diminished in the root zone ($Z/HR_{max} < 1$), where the frontal area was highest, and the velocity was enhanced above the root zone, where the frontal area was lowest. Local effects depending on the relative position with respect to mangroves can also be observed. For example, Figure 8a shows a significant velocity reduction as we move closer to the bottom for ADV3p4 and p5 measurements. However, that is not observed for ADV3p1, which is just behind one mangrove trunk.

The velocity near the water surface could not be captured, because the ADV cannot measure within 5 cm of the water surface. Then, to evaluate the depth-averaged velocity, uniform velocity in the region above the highest measurement point (where the ADV could not reach) was assumed. Because the model trees were identical and distributed in a regular array, the spatial variation in flow captured by the lateral profile shown (ADV3p1 to p5) should be representative of the velocity distribution around every tree in this array. We note that in the field, trees will not be identical, nor will they be distributed in a regular array, which would produce greater variability in the horizontal distribution of flow. To validate the uniform velocity assumption used to estimate local depth-averaged velocity, conservation of mass flux was evaluated between the upstream (ADV1) and the fully developed region (ADV3p1 to p5). This conservation of mass flux was evaluated for cases in which $h > HR_{max}$ and cases in which $h < HR_{max}$. For cases where $h > HR_{max}$, the channel-average velocity matched the upstream channel-average velocity to within 1%, satisfying conservation of mass. Therefore, for these cases the last velocity measurement, taken at the trunk level, can be considered as a good estimation of the velocity above that point. This makes sense, because in the region between the highest measurement point and the water surface the frontal area remains constant, so that a uniform velocity profile is expected. For cases where $h < HR_{max}$, the channel-average velocity under predicts the expected channel-average velocity by up to a 16%. In these cases, frontal area within the regions where velocity could not be measured

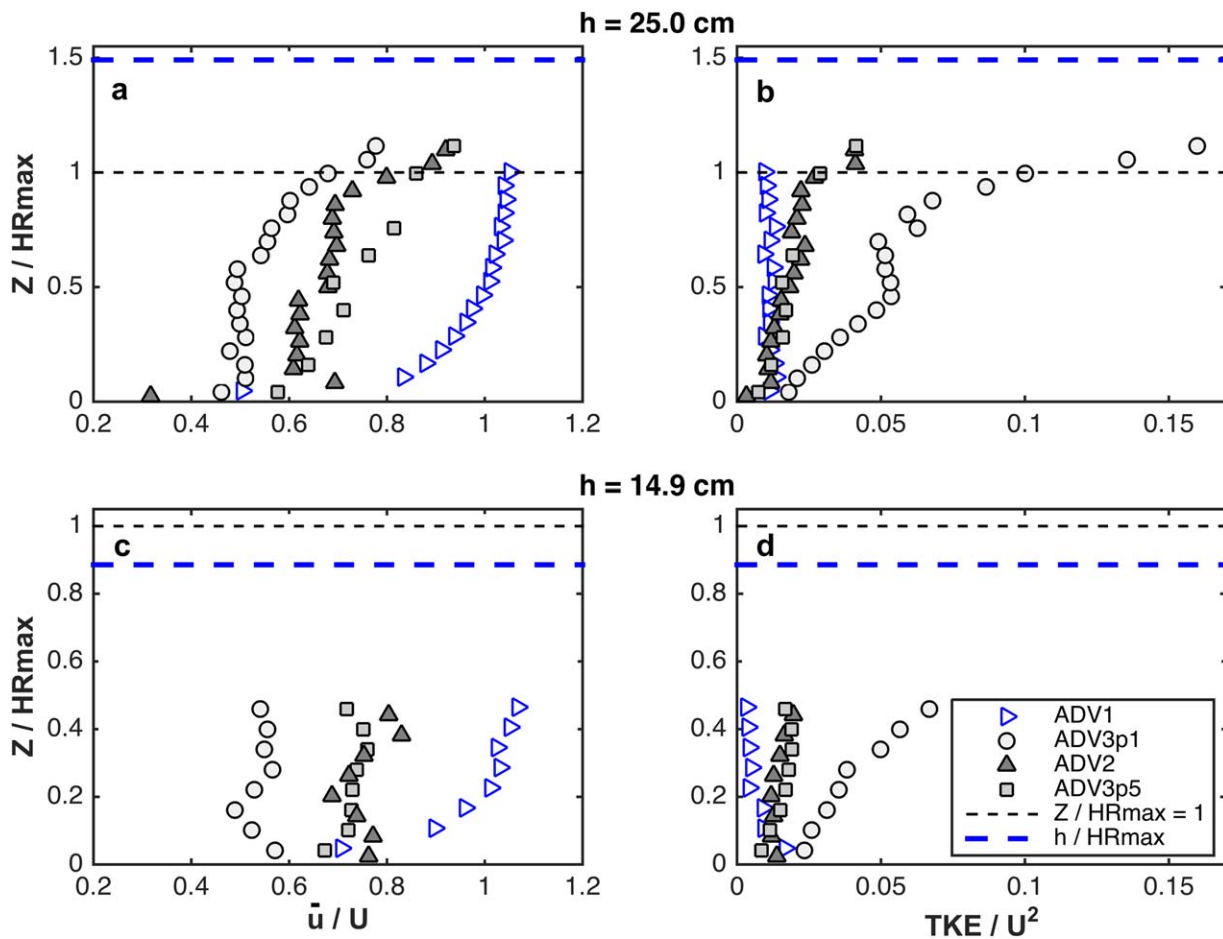


Figure 7. Time-averaged, streamwise velocity (left panels) and TKE (right panels) normalized by the channel-average velocity, U at different streamwise positions (see Figure 5). Plots a and b show results for $h = 25$ cm and $U = 9.0$ cm/s. Plots c and d show results for $h = 14.9$ cm and $U = 16.7$ cm/s. Measurements at the leading edge (blue triangles) are compared to profiles in the fully developed region (gray symbols) at different streamwise positions, all of which are aligned with the mangroves trunks. The location of the water surface is shown with blue dashed line.

decreases with increasing vertical position, since $h < HR_{max}$. It should be noted that, because of the parabolic shape of the roots, this frontal area variation is especially important in between trunk locations (see sketch in bottom plot of Figure 4 where different flow blockage areas are displayed). This distribution of frontal area suggests that the greatest increase in the velocity above the measured point would be produced in between the mangrove trunks. Therefore, the assumption of uniform velocity above the highest measurement point is most likely violated at the positions in between the mangrove trunks (positions ADV3p2, p3, and p4). However, at the positions in line with the mangrove trunks (positions ADV3p1, p5, and ADV2), this assumption is valid, because the vertical distribution of frontal area at this location is fairly uniform.

Second, the turbulence level was significantly enhanced within the mangrove forest, relative to the upstream condition (Figures 7b, 7d and 8b, 8d). For example, for $h = 25$ cm depth-averaged turbulent intensity at the leading edge of the forest was 8.5%. However, in the forest, the lateral-average of the multiple depth-averaged values (ADV3p1 to p5, Figure 8b) indicated a turbulent intensity equal to 18%, which was almost twice the turbulent intensity in an open channel flow (Nezu & Rodi, 1986). Vegetation can contribute two sources of turbulence (e.g., see discussions in Nepf and Vivoni 2000 and King et al. 2012). Turbulence can be generated in the wakes of individual roots and trunks. In addition, turbulence can be generated within shear-regions created by vertical variation in vegetation frontal area. Tanino and Nepf (2008) developed a model for the turbulence generated by element wakes by considering a balance between the production of turbulent kinetic energy and its viscous dissipation. For a sparse array of cylinders (which applies to this system),

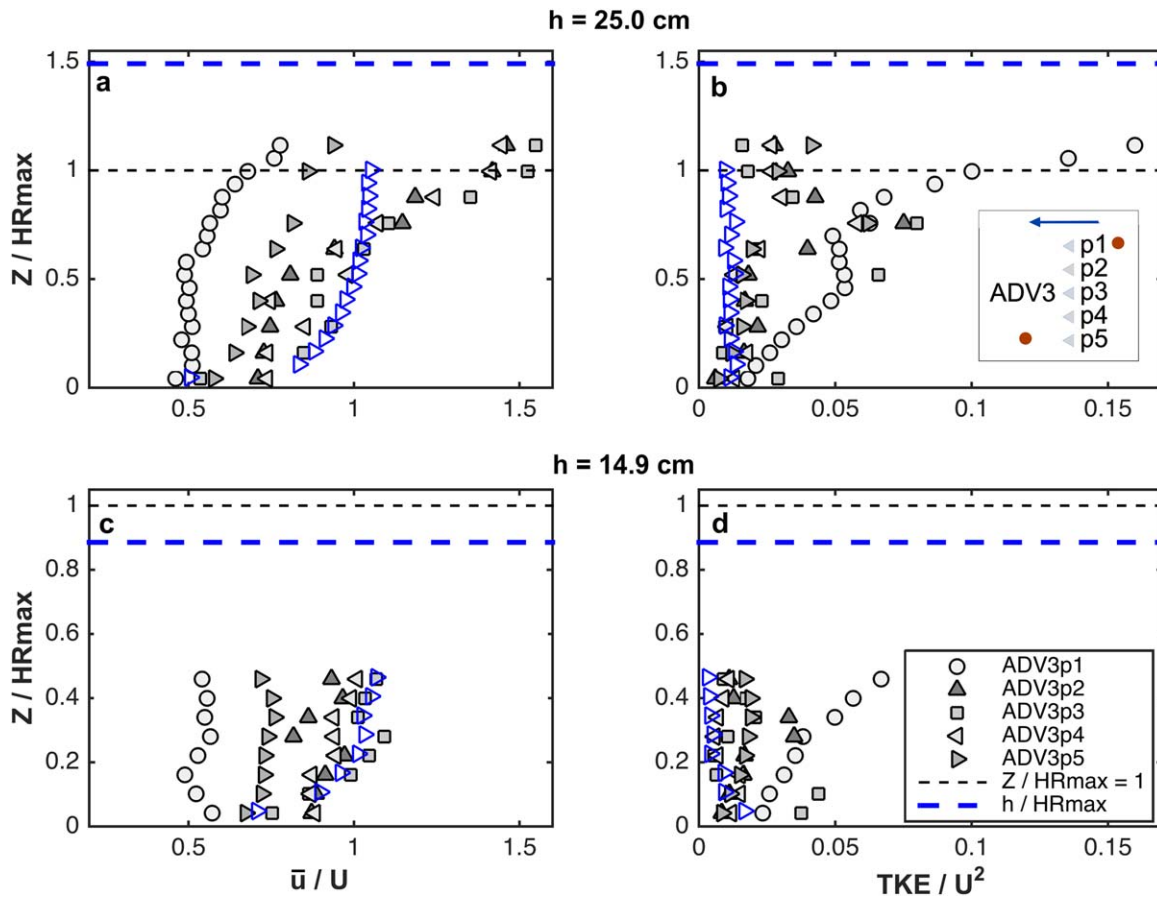


Figure 8. (left plots) Vertical profiles of time-averaged, streamwise velocity and (right plots) TKE normalized by the channel-average velocity U at different lateral positions (see Figure 5 and insert in plot b). Plots a and b show results for $h = 25$ cm and $U = 9.0$ cm/s. Plots c and d show results for $h = 14.9$ cm and $U = 16.7$ cm/s. Profiles at the leading edge (blue triangles) are compared to profiles in the fully developed region (gray symbols) at different lateral positions. Location of water surface is shown with blue dashed line.

$$\frac{\sqrt{\text{TKE}}}{U} = 1.1 \left[C_D \frac{\varphi}{(1-\varphi)\pi/2} \right]^{1/3} \quad (6)$$

This expression was verified for measurements up to a solid volume fraction of $\varphi = 0.06$ (Figure 14 in Tanino and Nepf 2008). Note that (6) assumes turbulent wakes, so that it is only valid for element Reynolds numbers, $Re = UD/\nu > 200$, with D the element diameter. Here we considered the application of (6) to the more complex configuration of the model mangrove. The drag coefficient, C_D , was taken from the force analysis described in section 3. The solid volume fraction was calculated by summing the root and trunk volume within the forest from the bed to the water surface and dividing by the total volume of the forest ($1 \text{ m} \times 2.5 \text{ m} \times h$) m^3 . For water depths $h = 25.0$ and 14.9 cm (Figures 7 and 8), $\varphi = 0.0037$ and 0.0044 , and $C_D = 1.13$ and 1.14 , respectively. Using equation (6), $\sqrt{\text{TKE}}/U = 0.15$ and 0.16 for $h = 25.0$ cm and 14.9 cm, respectively, corresponding to $(\text{TKE}/U^2) = 0.023$ and 0.026 , respectively. These values were in fairly good agreement with the TKE measured within the lower part of the root zone, e.g., $Z/HR_{\text{max}} < 0.5$ (Figures 7b, 7d and 8b, 8d). While lateral variation in TKE was observed, the average TKE level was consistent with that predicted from (6). Over a wider range of flow depth and velocity, with φ between 0.037 and 0.053 and h between 25 and 9 cm, respectively, we found that the measured spatial-averaged TKE in the bottom half of the root zone (TKE/U^2) differed from equation (6) by scale factor 0.55 ± 0.04 (95%CI), i.e., equation (6) over-predicted TKE by a factor of 2. This is fairly good agreement, given the simplicity of the formulation, indicating that equation (6) could be used to predict wake-generated TKE within more complex morphologies than a cylinder array. This relation could be used as a simple, subgrid scale model to predict TKE produced

by root and trunk wakes. In contrast, in the upper root zone and above the root zone, $Z/HR_{max} > 0.5$, the measured TKE exceeded that predicted by (6) for wake generation. The additional turbulence was likely contributed from local shear-production. For example, in the $h = 25$ cm case, the TKE was distinctly higher in the region $Z/HR_{max} > 0.5$ (Figures 7b and 8b), which corresponded to the region with significant vertical shear (Figures 7a and 8a). While shear was observed, we did not observe the formation of coherent structures via shear-instability. We believe these did not form because the shear-layer was not contiguous, as would be observed over a submerged canopy and for which these structures are consistently observed (e.g., Ghisalberti & Nepf 2006). While shear was observed in the individual velocity profiles, the vertical position of the shear zone was not uniform along the forest. Because of the parabolic root shape (Figure 3), the maximum height of roots was different at different horizontal positions, resulting in different vertical positions of the measured shear zone. This can be observed in Figures 7b and 8b, which show that the maximum shear and TKE were recorded at different heights according to the height reached by the roots at each horizontal position. In a real mangrove forest, the trees would be even more irregular and more irregularly spaced, so that a contiguous shear-layer at the top of the root layer would be even less likely.

In summary, the specific morphology of the mangrove led to a reduction of velocity near the bed, as flow was diverted to the region of lower frontal area away from the bed. A velocity reduction in the root zone can provide sheltered habit for nursery areas. The tendency for reduced near-bed velocity also suggests conditions that favor deposition and retention of fine particulate matter, which is linked to the already proven capacity for mangroves to build up soil (Furukawa & Wolanski, 1996; Krauss et al., 2003, 2010) and to provide CO_2 sequestration (Alongi 2014; Bouillon et al., 2008). However, the production of TKE in the wakes of roots and trunks enhanced the TKE within the model forest, relative to the bare bed (blue symbols in Figures 7 and 8). Elevated turbulence within the pneumatophores of a mangrove forest has also been observed in the field and attributed to root-wake generation (Mullarney et al., 2015). Mullarney et al. (2015) proposed that the root-generated TKE caused the observed reduction in fine sediment within the fringe mangrove, relative to adjacent regions. Similarly, stem-generated turbulence has been shown to inhibit deposition within regions of model vegetation in the laboratory (Chen et al., 2012; Liu & Nepf, 2016). Figures 7 and 8 highlight the potentially competing effects of mangrove root structure with regard to sediment retention, i.e., reduced near-bed velocity, but enhanced TKE. The root and trunk generation of turbulence is cut off once the root and trunk Reynolds numbers drop below ≈ 200 , and this threshold may be the key control between root zones that inhibit versus favor deposition (Liu & Nepf, 2016).

4.2. Forces Exerted on a Mangrove Located at the Leading Edge

Drag forces exerted on a mangrove located at the leading edge of the forest (position D01 in Figure 5) were obtained for different flow rates and for three depth ranges: $h_1 = 9.0\text{--}12.3$ cm, $h_2 = 13.3\text{--}14.2$ cm, and $h_3 = 20.3\text{--}25.0$ cm, corresponding to conditions with water depth both below and above the maximum root height ($HR_{max} = 16.8$ cm). As expected, the measured drag force increased with both channel velocity and water depth (Figure 9a). For each depth range, the measured forces were fitted to the following function of velocity, with coefficient α and exponent β :

$$F_D = \alpha U^\beta \tag{7}$$

The fitted models had high correlation coefficients, $\rho^2 > 0.975$, and the resulting exponents, β , were 2.10 ± 0.03 , 2.03 ± 0.02 , and 2.061 ± 0.001 for h_1 , h_2 , and h_3 , respectively. The fitted exponents agree with a quadratic drag law, $\beta = 2$, to within 5%, which can also be seen in the fit of measured forces as a function of U^2 (Figure 9c). Uncertainty introduced by frontal area, which was the main source of uncertainty, is represented by error bars.

The drag coefficient for each velocity and depth range was evaluated assuming the quadratic dependence demonstrated above.

$$C_D = \frac{2F_D}{\rho AU^2} \tag{8}$$

in which ρ is the fluid density, and A is the total mangrove frontal area, obtained as $A = \int_0^h dA(z)dz$, using the distribution of frontal area dA shown in Figure 3. The estimated drag coefficients are shown as a function of the trunk Reynolds number, $Re_{trunk} = UD_{trunk}/\nu$, in Figure 9b. Please recall that for root Reynolds

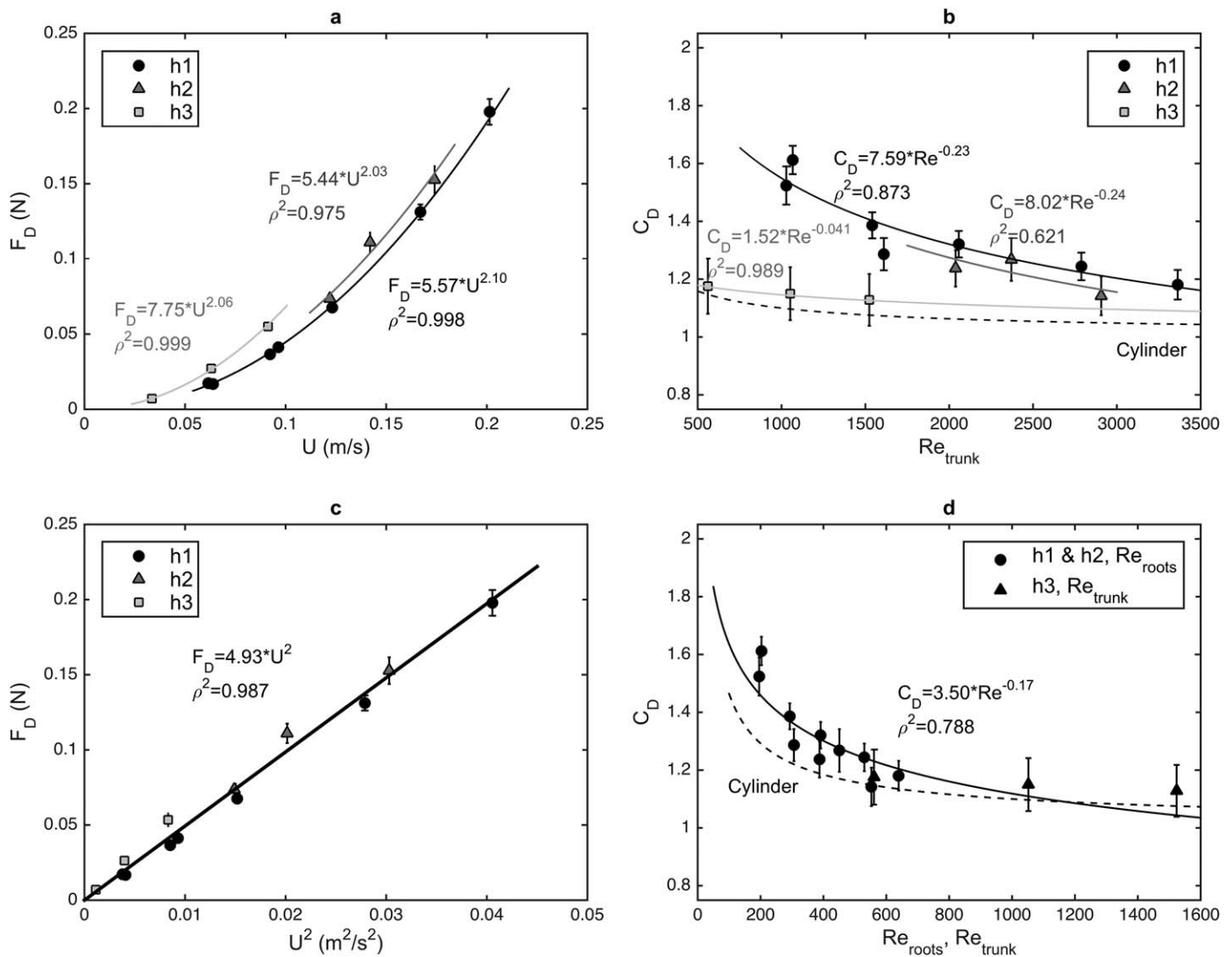


Figure 9. (a) and (c) Measured drag force as a function of channel-mean velocity for each of three flow depth ranges: $h_1 = 9.0$ – 12.3 cm, $h_2 = 13.3$ – 14.2 cm, and $h_3 = 20.3$ – 25.0 cm. (b) and (d) Drag coefficients estimated from equation (8). The error bars arise mainly from the uncertainty in frontal area (Figure 4). The trunk Reynolds number was defined as $Re_{trunk} = UD_{trunk}/\nu$ and the root Reynolds number was defined as $Re_{roots} = UD_{roots}/\nu$. The dashed line in plots (b) and (d) represent C_D for a smooth isolated cylinder with diameter defined as D_{trunk} .

number was below 200 the root wakes are not fully turbulent, and similarity to field conditions cannot be guaranteed. However, only two cases approached this limit. As a point of comparison, Figure 9b also includes the value of C_D for a smooth cylinder (White, 1991, dashed line in Figure 9). The estimated drag coefficients had a strong dependence on flow depth, with higher C_D for smaller flow depths. The cases in which the root zone occupied the entire flow depth (i.e., h_1 and $h_2 < HR_{max}$) exhibited similar fits (Figure 9b). However, cases for which the water depth extended above the root zone, i.e., $h_3 > HR_{max}$, exhibited lower drag coefficients at comparable velocity (comparable Re_{trunk}).

The depth dependence in C_D was likely associated with the different turbulence structures produced in each case. When $h < HR_{max}$ turbulence was dominated by wakes induced by mangrove roots, such that flow separation and vortex shedding scaled with the root diameter. Under these conditions, the characteristic length-scale to define inertial and viscous forces, and by extension Re , is the root diameter. On the other hand, when $h > HR_{max}$ a significant fraction of total drag was generated by the trunks above the root zone. In this region, the dominant drag length-scale was the trunk diameter, and a characterization by the trunk Reynolds number was appropriate. By characterizing the h_1 and h_2 cases with the root Reynolds number,

$Re_{\text{roots}} = UD_{\text{roots}}/\nu$, and the $h3$ cases with the trunk Reynolds number, $Re_{\text{trunk}} = UD_{\text{trunk}}/\nu$, the C_D values collapsed to a single function (Figure 9d), supporting our proposal. That is, when the flow was fully contained within the root zone, the appropriate drag length-scale was D_{root} but when a significant fraction of flow was above the root zone ($h > HR_{\text{max}}$), the drag length-scale shifted to D_{trunk} .

4.3. Drag Force Variation With Distance From Leading Edge

The change in drag force with distance from the leading edge was considered by comparing measurements at six locations along row D (Figure 5) with water depth ($h = 21.5\text{--}25$ cm) higher than the maximum root height. The force measured on an individual mangrove in the third row from the leading edge (D03) was comparable to that measured at the leading edge (D01), but beyond the third row the drag decreased by up to a 26% relative to the leading edge (Figure 10). Within uncertainty, the forces measured on individual mangroves were similar in all rows beyond the fifth tree row, which corresponded to the distance 0.85 m from the leading edge. Previous studies note that the adjustment length for flow through a sparse, submerged (or finite width) canopy can be described by the drag length-scale, $(C_D a)^{-1}$ (Coceal & Belcher, 2004; Rominger & Nepf, 2011). Strictly, this describes the distance required for flow to be redirected from the canopy to an unvegetated adjacent region. Here the canopy was not submerged and all regions of the flow were occupied by vegetation, although with variable a , so that this formulation may not apply. However, depth averaging a from 0 to HR_{max} produced a root-zone average of $a = 0.80 \text{ m}^{-1}$, and then $1/(C_D a) = 0.96 \text{ m}$, which was close to the adjustment length-scale obtained from the velocity measurements (0.85 m). This indicated that the adjustment-scale $1/(C_D a)$ considering the average a within the highest flow blockage region, i.e., the root zone, can apply in this case.

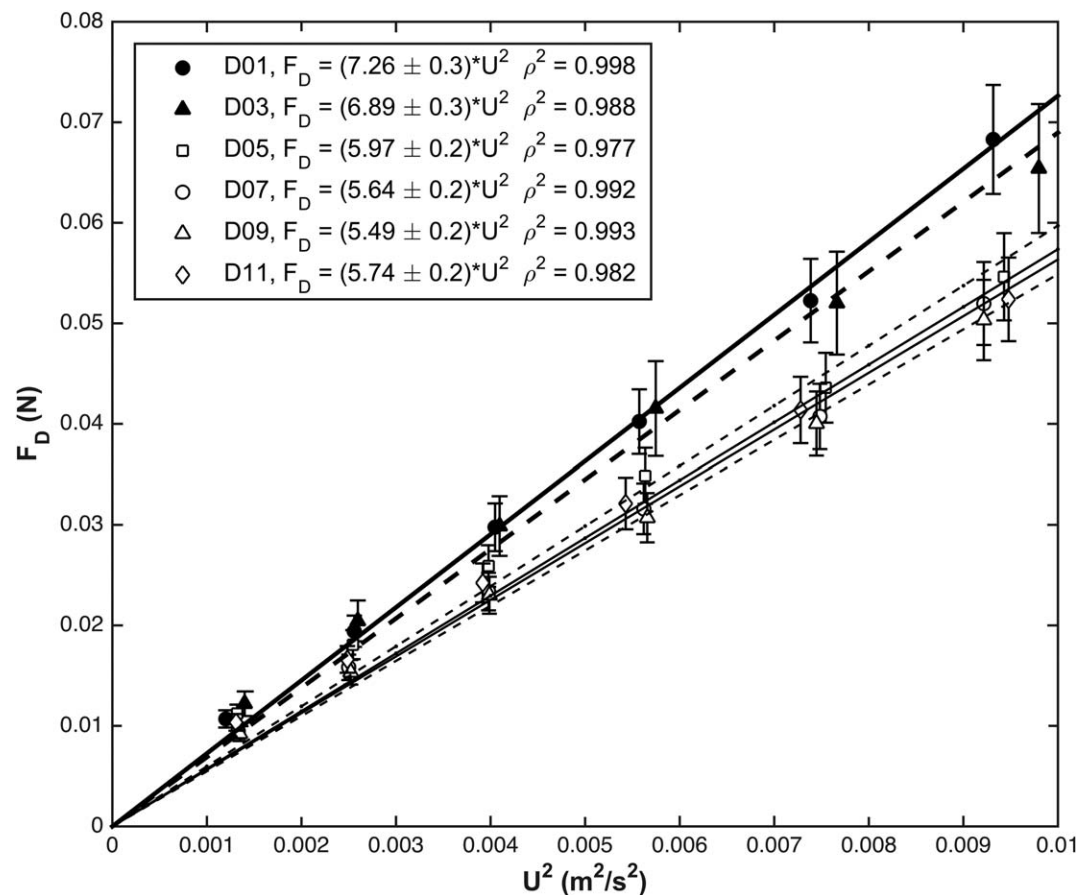


Figure 10. Drag forces measured at positions with increasing distance from the leading edge as a function of the velocity squared. Measurements were made at rows 1, 3, 5, 7, 9, and 11, as shown in Figure 5. In all cases included here the water depth ($h = 21.5\text{--}25$ cm) was higher than the maximum root height.

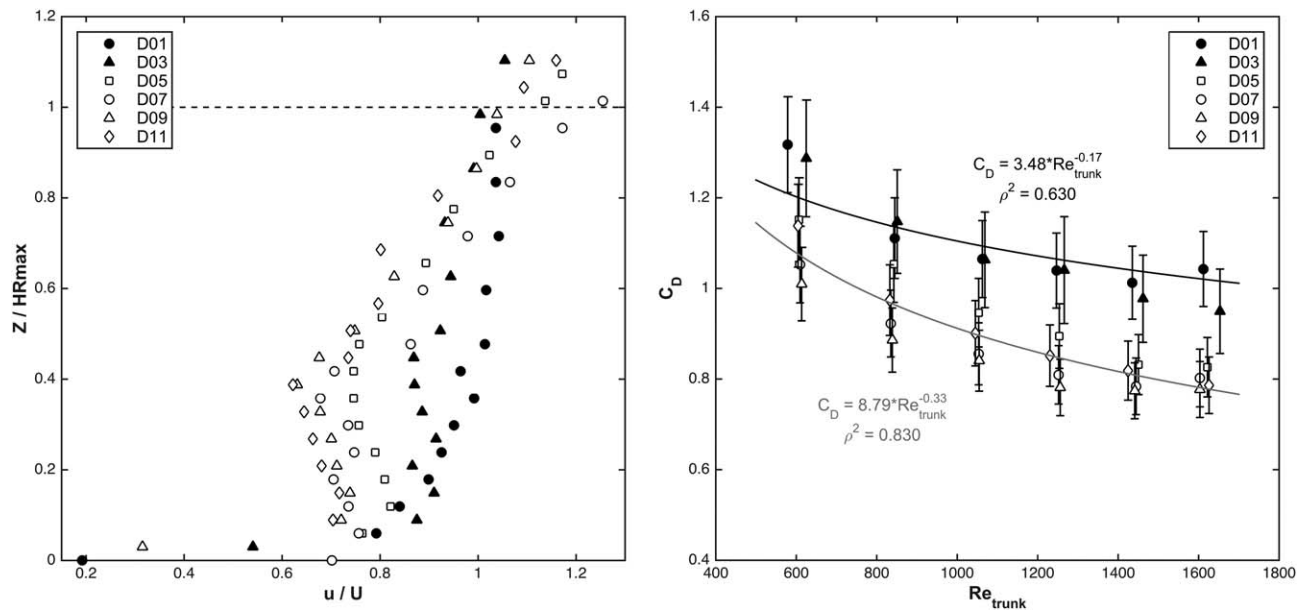


Figure 11. (left plot) Velocity profiles measured at mangrove positions D01, D03, D05, D07, D09, and D11 and drag coefficients for those mangroves as a function of Re_{trunk} .

The reduction in drag can be explained by the redistribution of velocity in both the vertical and horizontal directions that occurred in response to the mangrove trees. At the leading edge the velocity profile was nearly uniform, except close to the bed (black circles in Figure 11a). Moving into the forest, the velocity decreased in the root zone ($Z/HR_{max} < 1$, Figure 11a) where the frontal area was higher, and the velocity increased above the root zone where the frontal area was lower. Since drag is proportional to both frontal area and velocity squared, a flow adjustment that leads to higher velocity in the region of lower frontal area should lead to an overall reduction in drag. The velocity also redistributed in the horizontal plane. Specifically, the velocity in line with the trunks was significantly diminished relative to the channel-average (see ADV3p1 and ADVp5 in Figure 8). A lower velocity in line with the trees would also reduce the force on the tree. The bulk of the velocity adjustment occurred between the leading edge (D01, black circles in Figure 11a) and row D05 (white squares in Figure 11a), which was consistent with the distance over which the drag force changed (Figure 10). In addition, the drag was reduced, relative to the leading edge, in row D05 and beyond for all velocities tested, suggesting that flow adjustment length from the leading edge is not dependent on velocity. Due to the flow redistribution and because the drag coefficients estimated from (8) used the channel-average velocity, which does not account for the velocity redistribution, the drag coefficients estimated in row D05 and beyond were diminished relative to the drag coefficient at the leading edge (Figure 11b).

A decrease in force after the row of a forest model has been previously reported by Maza et al. (2015), in a numerical study of solitary waves interacting with a cylinder array. The solitary wave height was reduced with distance from the array leading edge, which partially explained the reduction in wave-exerted forces. However, the wave height decay was almost linear along the array (Figure 14 in Maza et al., 2015), whereas the forces declined in a nonlinear way, with a larger reduction within the first row and then a much slower decline in force with further distance from the leading edge (Figure 15 in Maza et al., 2015). This indicated that the force evolution along the forest was not driven solely by wave decay, but also by the redistribution of the velocity field. In this case, with vertically uniform cylinders, flow redistribution occurred in only the lateral direction. Specifically, velocity was reduced in-line with the cylinder rows, reducing the force on the cylinders.

To assess the relative importance of lateral and horizontal velocity reconfiguration on tree force, the drag coefficient was recalculated using the local depth-averaged velocity, rather than the channel-average velocity, U . Specifically, the local depth-averaged velocity, U_{xy} , was obtained using ADV measurements at each

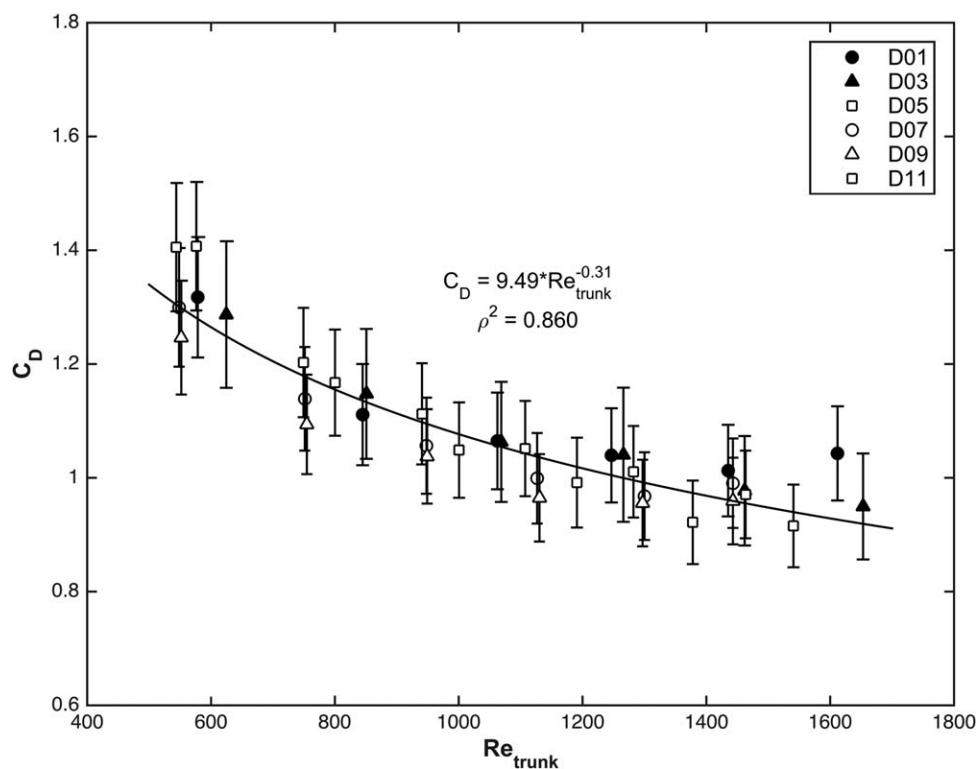


Figure 12. Drag coefficients obtained considering the local depth-averaged velocity, U_{xy} , instead of the channel-average velocity, U , in equation (8) plotted as a function of $Re_{trunk} = U_{xy}D_{trunk}/\nu$. A common fitting for all data is shown in the figure.

location along the forest (D01–D11, Figure 5). The subscript xy was used to highlight that the local depth-average velocity varied in the horizontal plane (e.g., see Figure 8). Because the ADV could not record velocity within 5 cm of the free surface, velocity in this region was estimated as being equal to the velocity recorded at the point nearest to the free surface. The values of local depth-averaged velocity measured at the tree positions were lower than the channel-average ($U_{xy} < U$). This was due to the lateral redirection of velocity, as illustrated in Figure 8. New estimates of C_D were obtained by substituting U_{xy} into equation (8). When plotted as a function of trunk Reynolds number defined using U_{xy} , the new drag coefficients collapsed to a common fitting (Figure 12), $C_D = 9.49Re_{trunk}^{-0.31}$. That is, by correcting for the velocity redistribution in the horizontal plane, the drag coefficient lost its dependence on distance from the leading edge. This suggested that the flow redistribution in the horizontal plane was the more significant contributor to the reduction in C_D estimated with the channel-average velocity. If the local, depth-average velocity can be resolved within a numerical model, e.g., when using a point-drag representation for the trees, this single drag coefficient relation (Figure 12) can be used to calculate the appropriate drag at any location within the forest. However, for numerical models in which flow is not resolved within the forest (e.g., using a distributed drag approach), the previous formulations (Figure 11) should be used to estimate drag forces at different distances from the leading edge, based on the channel-average velocity.

5. Conclusions

A mangrove forest model based on the *Rhizophora* morphology was built at 1/12th scale. Each model tree included 24 prop roots distributed in a three-dimensional layout. The velocity and forces on individual trees were measured at the forest leading edge and within the fully developed region of the forest at channel-average flow speeds of 3–20 cm/s and water depths between 9 and 25 cm, which correspond to speeds of 0.10–0.69 cm/s and water depths of 1.1 and 3.0 m at real scale. The velocity field evolved from a boundary layer profile at the forest leading edge to a profile determined by the vertical distribution of frontal area, with significantly higher velocity measured above the root zone. In addition, the velocity field also adjusted

in the horizontal plane, with significantly lower velocity in line with the trunks. The fully developed conditions were reached at the fifth tree row from the leading edge. Within the lower root zone nearest the bed, where frontal area was highest, the velocity was reduced by up to 50% and the TKE was increased by as much as fivefold, relative to the upstream conditions. The increase in TKE within the root zone was attributed to two sources. First, the contribution from turbulent wakes generated by individual trunk and roots dominated near the bed, and measured values of TKE near the bed agreed with existing models that predict turbulence generation by individual vegetative elements. A second source of turbulence came from the velocity shear generated by the sharp decrease in frontal area at the top of the root zone. The enhanced near-bed TKE could locally inhibit the deposition of fine particulate matter within the forest, which is counter to the prevailing expectation of sediment retention within a forest.

The drag exhibited a quadratic dependence on velocity, which justified the definition of a quadratic drag coefficient. The measured drag coefficients collapsed to a single function of Reynolds number only after the correct length-scale for drag was identified. The dominant drag length-scale was dependent on flow depth. Specifically, for flow contained fully within the root zone ($h < HR_{max}$), the drag length-scale was the root diameter, but for flow distributed partly above the root zone ($h > HR_{max}$) the drag length-scale was the trunk diameter. Forces measured on individual mangroves, and the drag coefficients defined using the channel-average velocity, $U = Q/(Bh)$, decreased from the leading edge, but reached an almost constant force at the fifth tree row, consistent with the velocity reaching its fully developed profile at the fifth tree row. The decrease in drag from the leading edge was predominantly associated with the lateral redistribution of flow, with significantly lower velocity measured in line with the trunks. Consistent with this, C_D values estimated using the local depth-average velocity, U_{xy} , which accounted for the lateral flow reconfiguration, exhibited no dependence with distance from the leading edge.

Acknowledgments

M. Maza is indebted to the MEC (Ministerio de Educación, Cultura y Deporte, Spain) for the funding provided in the Traslados Temporales funding associated to FPU (Formación del Profesorado Universitario) studentship (BOE-A-2012-6238). Funds also provided by Donald and Martha Harleman Research Fund. K. Adler and A. M. García were supported by the MIT Undergraduate Research Opportunities Program (UROP) and the MIT Summer Research Program, respectively. Supporting data are included as an XLSX file named Maza-ds01.

References

- Alongi, D. M. (2008). Mangrove forests: Resilience, protection from tsunamis, and responses to global climate change. *Estuarine, Coastal and Shelf Science*, *76*, 1–13.
- Alongi, D. M. (2014). Carbon cycling and storage in mangrove forests. *Annual Review of Marine Science*, *6*, 195–219.
- Barbier, E. B., Hacker, S. D., Kennedy, C., Koch, E. W., Stier, A. C., & Silliman, B. R. (2011). The value of estuarine and coastal ecosystem services. *Ecological Monographs*, *81*, 169–193.
- Ba Thuy, N., Tanimoto, K., Tanaka, N., Harada, K., & Iimura, K. (2009). Effect of open gap in coastal forest on tsunami run up—Investigations by experiment and numerical simulation. *Ocean Engineering*, *36*, 1258–1269.
- Bouillon, S., Borges, A. V., Castañeda-Moya, E., Diele, K., Dittmar, T., Duke, N. C., . . . Twilley, R. R. (2008). Mangrove production and carbon sinks: A revision of global budget estimates. *Global Biogeochemical Cycles*, *22*, GB2013. <https://doi.org/10.1029/2007GB003052>
- Chen, Z., Ortiz, A., Zong, L., & Nepf, H. (2012). The wake structure behind a porous obstruction and its implications for deposition near a finite patch of emergent vegetation. *Water Resources Research*, *48*, W09517. <https://doi.org/10.1029/2012WR012224>
- Coccal, O., & Belcher, S. (2004). A canopy model of mean winds through urban areas. *Quarterly Journal of the Royal Meteorological Society*, *130*(599), 1349–1372.
- Dalrymple, R. A., Kirby, J. T., & Hwang, P. A. (1984). Wave Diffraction Due to Areas of Energy Dissipation. *Journal of Waterway Port, Coastal, and Ocean Engineering*, *110*, 67–79.
- de Groot, R., Brander, L., van der Ploeg, S., Costanza, R., Bernard, F., Braat, L., . . . van Beukering, P. (2012). Global estimates of the value of ecosystems and their services in monetary units. *Ecosystem Services*, *1*, 50–61.
- Furukawa, K., & Wolanski, E. (1996). Sedimentation in mangrove forests. *Mangroves and Salt Marshes*, *1*, 3–10.
- Ghisalberti, M., & Nepf, H. (2006). The structure of the shear layer over rigid and flexible canopies. *Environmental Fluid Mechanics*, *6*(3), 277–301.
- Goring, D. G., & Nikora, V. I. (2002). Despiking acoustic Doppler velocimeter data. *Journal of Hydraulic Engineering*, *128*(1), 117–126.
- Huang, Z., Yao, Y., Sim, S. Y., & Yao, Y. (2011). Interaction of solitary waves with emergent, rigid vegetation. *Ocean Engineering*, *38*, 1080–1088.
- IPCC Working Group II (2014). *Climate change 2014: Impacts, adaptation, and vulnerability*. Philadelphia, PA: W. B. Saunders. Retrieved from www.ipcc.ch/report/ar5/wg2/
- Irttem, E., Gedik, N., Kabdasli, M. S., & Yasa, N. E. (2009). Coastal forest effects on tsunami run-up heights. *Ocean Engineering*, *36*, 313–320.
- Ismail, H., Abd Wahab, A. K., & Alias, N. E. (2012). Determination of mangrove forest performance in reducing tsunami run-up using physical models. *Natural Hazards*, *63*, 939–963.
- King, A. T., Tinoco, R. O., & Cowen, E. A. (2012). A k-ε turbulence model based on the scales of vertical shear and stem wakes valid for emergent and submerged vegetated flows. *Journal of Fluid Mechanics*, *701*, 1–39.
- Kobayashi, N., Raichle, A. W., & Asano, T. (1993). Wave attenuation by vegetation. *Journal of Waterway Port, Coastal, and Ocean Engineering*, *119*(1), 30–48.
- Krauss, K. W., Allen, J. A., & Cahoon, D. R. (2003). Differential rates of vertical accretion and elevation change among aerial root types in Micronesian mangrove forests. *Estuarine, Coastal and Shelf Science*, *56*, 251–259.
- Krauss, K. W., Cahoon, D. R., Allen, J. A., Ewel, K. C., Lynch, J. C., & Cormier, N. (2010). Surface elevation change and susceptibility of different mangrove zones to sea-level rise on Pacific high islands of Micronesia. *Ecosystems*, *13*, 129–143.
- Liu, C., & Nepf, H. (2016). Sediment deposition within and around a finite patch of model vegetation over a range of channel velocity. *Water Resources Research*, *51*, 600–612. <https://doi.org/10.1002/2015WR018249>
- Losada, I. J., Maza, M., & Lara, J. L. (2016). A new formulation for vegetation-induced damping under combined waves and currents. *Coastal Engineering*, *107*, 1–13.

- Maza, M., Lara, J. L., & Losada, I. J. (2015). Tsunami wave interaction with mangrove forests: A 3-D numerical approach. *Coastal Engineering*, 98, 33–54.
- Mazda, Y., Wolanski, E., King, B., Sase, A., Ohtsuka, D., & Magi, M. (1997). Drag force due to vegetation in mangrove swamps. *Mangroves and Salt Marshes*, 1, 193–199.
- Méndez, F. J., Losada, I. J., & Losada, M. A. (1999). Hydrodynamics induced by wind waves in a vegetation field. *Journal of Geophysical Research*, 104, 18383–18396.
- Méndez-Alonzo, R., Moctezuma, C., Ordoñez, V. R., Angeles, G., Martínez, A. J., & López-Portillo, J. (2015). Root biomechanics in Rhizophora mangle: Anatomy, morphology and ecology of mangrove's flying buttresses. *Annals of Botany*, 115(5), 833–840.
- Mitsch, W. J., & Gosselink, J. G. (2015). *Wetlands* (5th ed.). Hoboken, NJ: Wiley.
- Mullarney, J. C., Norris, B. K., Henderson, S. M., & Bryan, K. R. (2015). *Finescale turbulence and seabed scouring around pneumatophores in a wave-exposed mangrove forest*. Abstract #EP21D-02 presented at the 2015 AGU Fall Meeting, San Francisco, USA.
- Munson, B., Rothmayer, Okiishi, A., & Huebsch, T. W. (2013). *Fundamentals of Fluid Mechanics* (7th ed.). Hoboken, NJ: John Wiley and Sons.
- Narayan, S., Beck, M. W., Reguero, B. G., Losada, I. J., van Wesenbeeck, B., Pontee, N., . . . Burks-Copes, K. A. (2016). The effectiveness, costs and coastal protection benefits of natural and nature-based defenses. *PLoS ONE*, 11(5), e0154735. <https://doi.org/10.1371/journal.pone.0154735>
- Nepf, H., & Vivoni, E. (2000). Flow structure in depth-limited, vegetated flow. *Journal of Geophysical Research*, 105, 28547–28557.
- Nezu, I., & Rodi, W. (1986). Open channel flow measurements with a laser Doppler anemometer. *Journal of Hydraulic Engineering*, 112(5), 335–355.
- Ohira, W., Honda, K., Nagai, M., & Ratanasuwana, A. (2013). Mangrove stilt root morphology modelling for estimating hydraulic drag in tsunami inundation simulation. *Trees*, 27, 141–148.
- Roeber, V., & Bricker, J. D. (2015). Destructive tsunami-like wave generated by surf beat over a coral reef during Typhoon Haiyan. *Nature Communications*, 6, 7854.
- Rominger, J., & Nepf, H. (2011). Flow adjustment and interior flow associated with a rectangular porous obstruction. *Journal of Fluid Mechanics*, 680, 636–659.
- Strusinska-Correia, A., Husrin, S., & Oumeraci, H. (2013). Tsunami damping by mangrove forest: A laboratory parameterized trees. *Natural Hazards and Earth System Sciences*, 13, 483–503.
- Sutton-Grier, A., Wowk, K., & Balmford, H. (2015). The potential for natural and hybrid infrastructure to enhance the resilience of our coastal communities, economies and ecosystems. *Environment Science and Policy*, 51, 137–148.
- Tanino, Y., & Nepf, H. (2008). Laboratory investigation on mean drag in a random array of rigid, emergent cylinders. *Journal of Hydraulic Engineering*, 134, 34–41.
- Vo-Luong, H. P., & Massel, S. R. (2008). Energy dissipation in non-uniform mangrove forests of arbitrary depth. *Journal of Marine Systems*, 74, 603–622.
- Ward, G. A., Smith, T. J., Whelan, K. R. T., & Doyle, T. W. (2006). Regional processes in mangrove ecosystems: spatial scaling relationships, biomass, and turn-over rates following catastrophic disturbance. *Hydrobiologia*, 569, 517–527.
- White, F. M. (1991). *Viscous fluid flow* (2nd ed., 614 pp.). New York, NY: McGraw-Hill.
- Yanagisawa, H., Koshimura, S., Goto, K., Miyagi, T., Imamura, F., Ruangrassamee, A., & Tanavud, C. (2009). The reduction effects of mangrove forest on a tsunami based on field surveys at Pakarang Cape, Thailand and numerical analysis. *Estuarine, Coastal and Shelf Science*, 81, 27–37.
- Zhang, X., Chua, V. P., & Cheonf, H. F. (2015). Hydrodynamics in mangrove prop roots and their physical properties. *Journal of Hydro-Environment Research*, 9, 281–294.